



Determining the Dominant Acceleration Mechanism during Relativistic Magnetic Reconnection in Large-scale Systems

Fan Guo¹ , Xiaocan Li¹, William Daughton¹ , Patrick Kilian¹ , Hui Li¹ , Yi-Hsin Liu², Wangcheng Yan³, and Dylan Ma¹

¹Los Alamos National Laboratory, NM 87545, USA

²Dartmouth College, Hanover, NH 03750, USA

³The University of Tennessee, Knoxville, TN 37996, USA

Received 2019 March 16; revised 2019 June 10; accepted 2019 June 14; published 2019 July 10

Abstract

While a growing body of research indicates that relativistic magnetic reconnection is a prodigious source of particle acceleration in high-energy astrophysical systems, the dominant acceleration mechanism remains controversial. Using a combination of fully kinetic simulations and theoretical analysis, we demonstrate that Fermi-type acceleration within the large-scale motional electric fields dominates over direct acceleration from non-ideal electric fields within small-scale diffusion regions. This result has profound implications for modeling particle acceleration in large-scale astrophysical problems, as it opens up the possibility of modeling the energetic spectra without resolving microscopic diffusion regions.

Key words: acceleration of particles – galaxies: jets – magnetic reconnection – relativistic processes – gamma-ray burst: general – pulsars: general

1. Introduction

Magnetic reconnection is a plasma process that rapidly unleashes energy stored in magnetic shear into various forms of particle kinetic energy. It has been discussed in solar and space environments (Kopp & Pneuman 1976; Phan et al. 2000), laboratory experiments (Ji et al. 1998), and recently in the context of high-energy astrophysics (de Gouveia dal Pino & Lazarian 2005; Giannios et al. 2009; Zhang & Yan 2011; Arons 2012; Hoshino & Lyubarsky 2012; McKinney & Uzdensky 2012; Zhang et al. 2015, 2018). There is strong observational evidence suggesting that reconnection is an efficient process for producing energetic particles in various heliophysics and astrophysical systems (Øieroset et al. 2002; Krucker et al. 2010; Abdo et al. 2011; Tavani et al. 2011; Birn et al. 2012; Gary et al. 2018; Oka et al. 2018). However, the acceleration physics remains an area of active research.

Recently, a growing body of research indicates that relativistic magnetic reconnection in the magnetically dominated regime (magnetization parameter $\sigma = B^2/(4\pi nmc^2) \gg 1$) is a prodigious source of high-energy particles in various astrophysical systems. However, the dominant acceleration mechanism remains controversial. Two identified candidates are direct acceleration at diffusion regions surrounding X-lines (Zenitani & Hoshino 2001; Fu et al. 2006; Pritchett 2006; Uzdensky et al. 2011; Cerutti et al. 2013; Sironi & Spitkovsky 2014; Wang et al. 2016), and Fermi-type acceleration within the much larger-scale reconnection layer (Drake et al. 2006; Oka et al. 2010; Bessho & Bhattacharjee 2012; Dahlin et al. 2014; Guo et al. 2014, 2015; Li et al. 2017, 2018a). An additional controversy is the roles of the two mechanisms in producing the power-law particle energy distribution (Guo et al. 2014, 2015; Sironi & Spitkovsky 2014; Werner et al. 2016). Sironi & Spitkovsky (2014) have proposed that the power-law shape is established as the particles interact with the X-points (more specifically, diffusion regions with weak magnetic field $|E| > |B|$) through direct acceleration (Zenitani & Hoshino 2001). They argue that this process is essential for the formation of power-law distributions and it

determines the spectral index of the energy spectra. In contrast, Guo et al. (2014, 2015) proposed that the power-law distributions are produced by a Fermi-like process and continuous injection from the reconnection inflow. Based on this idea, they developed a theoretical model that is consistent with the hard spectra $f \propto \varepsilon^{-p}$ observed in simulations (approaching $p = 1$, where p in the power-law index).

Determining the dominant acceleration mechanism and formation of power-law distribution in kinetic simulations is vital for understanding and building reconnection acceleration models for large-scale applications. Because of the enormous scale separation between the system size and the skin depth scale ($L/\lambda_e \sim 10^8$ for solar flares, $\sim 10^{13}$ for PWNe, and $\sim 10^{17}$ for extragalactic jets; Ji & Daughton 2011), it is impractical for conventional kinetic simulation methods to model the whole problem. There have been attempts for modeling particle acceleration during magnetic reconnection in a macroscopic system by neglecting acceleration due to the non-ideal electric field (le Roux et al. 2015; Beresnyak & Li 2016; Li et al. 2018b; Drake et al. 2019). To assess these models, it is important to determine if the non-ideal electric field plays any significant role in large-scale reconnection acceleration. The focus of this Letter is to distinguish the acceleration mechanisms and their roles in the development of the nonthermal power-law spectrum. Through a combination of fully kinetic simulations and theoretical analysis, we demonstrate that the dominant acceleration mechanism is a Fermi-type process in the motional electric field induced from plasma motion in the reconnection layer. While the non-ideal electric field may act as an additional particle injection for further Fermi acceleration, it is not necessary for the formation of power-law distributions and therefore can be neglected when modeling the energetic particle spectra in large-scale astrophysical reconnection events.

2. Numerical Simulations

Simulations start from a force-free current layer with $\mathbf{B} = B_0 \tanh(z/\lambda)\hat{x} + B_0 \operatorname{sech}(z/\lambda)\hat{y}$, corresponding to a

magnetic field rotating by 180° across the sheet. The plasma consists of electron–positron pairs (mass ratio $m_p/m_e = 1$). The initial distributions are Maxwellian with a uniform density n_0 and temperature ($T_p = T_e$). For the simulations presented here, the thermal energy per particle is $0.36m_e c^2$, but we have verified that our main conclusion is valid even when T_p is as low as $0.01m_e c^2$. Particles in the sheet have a drift velocity $\mathbf{u}_p = -\mathbf{u}_e$, and that gives rise to a current density satisfying Ampere’s law $\nabla \times \mathbf{B} = 4\pi \mathbf{J}$. The simulations are performed using the VPIC (Bowers et al. 2008) and NPIC codes (Daughton et al. 2006; Daughton & Karimabadi 2007), both of which solve the relativistic Vlasov–Maxwell equations but use different methods for solving the equations. We focus on the case with $\sigma_e = B^2/(4\pi n_e m_e c^2) = 100$ ($\sigma = 50$ including both species), corresponding to $\omega_{pe}/\Omega_{ce} = 0.1$, where ω_{pe} is the plasma frequency and Ω_{ce} is the electron gyrofrequency. Results for different σ and domain size will be published elsewhere. The electric and magnetic fields are normalized by B_0 . The domain size is $L_x \times L_z = 600d_e \times 400d_e$, where $d_e = c/\omega_{pe} = c/(4\pi n_e e^2/m_e)^{1/2}$ is the inertial length (without relativistic correction). The resolution of the simulations is $N_x \times N_z = 3072 \times 2048$. All simulations used more than 100 particles per species per cell for each species, employed periodic boundary conditions in the x -directions, and in the z -direction used conducting boundaries for the fields and reflecting boundaries for the particles. The half-thickness is $\lambda = 6d_e$. A small long-wavelength perturbation is included to initiate reconnection.

In VPIC simulations, we have developed a particle-tracing module to output particle trajectories and find the electric field, magnetic field, and bulk fluid velocity at particle locations for studying particle energization (Guo et al. 2016; Li et al. 2018a, 2019). In this study, we uniformly select ~ 1 million particles in the beginning of the simulation and analyze their acceleration to high energy. In order to definitely demonstrate the acceleration physics, we developed the capability of including test particles that interact with magnetic fields in the normal manner, but only interact with the motional electric field $\mathbf{E}_m = -\mathbf{u} \times \mathbf{B}/c$, and do not experience any non-ideal electric fields. Note that because this technique requires us to calculate plasma flow velocity \mathbf{u} from a finite number of particles, it introduces additional numerical noise to the test-particle component. For these simulations we use more self-consistent particles 1200 per cell per species in the initial setup. We also tag particles when they reached a region with weak magnetic field $|E| > |B|$, which is emphasized by Sironi & Spitkovsky (2014). Our earlier studies have shown that VPIC and NPIC give consistent results and we present results from the two codes without distinction.

3. Distinguishing the Acceleration Mechanisms

We attempt to distinguish two types of processes: the Fermi-type acceleration process in reconnection-driven bulk flows, and direct acceleration in diffusion regions. While the Fermi-type acceleration is accomplished in the electric field induced by bulk plasma motion $\mathbf{E}_m = -\mathbf{u} \times \mathbf{B}/c$, the non-ideal electric field that is associated with direct acceleration can be distinguished by the generalized Ohm’s law (Bessho & Bhattacharjee 2005; Hesse & Zenitani 2007; Swisdak et al.

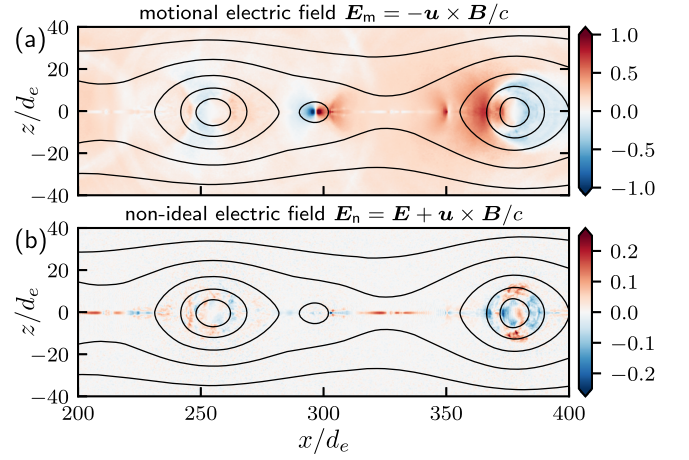


Figure 1. Distribution of y -components of (a) motional electric field, and (b) non-ideal electric field normalized by B_0 at $\omega_{pe}t = 400$ overlaid by the contours representing magnetic field lines.

2008; Liu et al. 2015)

$$\begin{aligned} \mathbf{E} = & -\frac{\mathbf{u} \times \mathbf{B}}{c} + \frac{1}{ne} \nabla \cdot (\mathbf{P}_p - \mathbf{P}_e) \\ & + \frac{m_e}{ne} \left[n_p \left(\frac{\partial \mathbf{w}_p}{\partial t} + \mathbf{u}_p \cdot \nabla \mathbf{w}_p \right) \right. \\ & \left. - n_e \left(\frac{\partial \mathbf{w}_e}{\partial t} + \mathbf{u}_e \cdot \nabla \mathbf{w}_e \right) \right], \end{aligned} \quad (1)$$

where $n = n_p + n_e$ and we have assumed a pair plasma $m_p = m_e$ so the Hall term vanishes. \mathbf{P}_p and \mathbf{P}_e are pressure tensors for the two particle species. \mathbf{w}_p and \mathbf{w}_e are moments of the space-like components of the four velocity for each species, respectively (Hesse & Zenitani 2007; Liu et al. 2015). Different from some earlier analysis (Bessho & Bhattacharjee 2005; Swisdak et al. 2008), the charge neutrality assumption is dropped as local charge separation during relativistic reconnection can be quite large.

Based on Equation (1), for each tracer particle one can distinguish the Fermi-like acceleration by calculating energy gain $\Delta \varepsilon_m = \int \mathbf{q} \mathbf{v} \cdot \mathbf{E}_m dt$, where \mathbf{v} is the particle velocity, from the acceleration by the non-ideal electric field $\Delta \varepsilon_n = \int \mathbf{q} \mathbf{v} \cdot \mathbf{E}_n dt = \int \mathbf{q} \mathbf{v} \cdot (\mathbf{E} + \mathbf{u} \times \mathbf{B}/c) dt$ including the direct acceleration at X-line regions. In addition, we tag particles that entered diffusion regions with a strong electric field and weak magnetic field $|E| > |B|$ at least once, and calculate their energy distributions in the diffusion region and how they evolve elsewhere in the simulation domain.

4. Simulation Results

Figure 1 contrasts y -components of motional electric field E_{my} and non-ideal electric field E_{ny} in the simulation at $\omega_{pe}t = 400$. To better illustrate the fine-scale structure of the non-ideal electric field, both panels are magnified to the region $200 < x/d_e < 400$ and $-40 < z/d_e < 40$. The motional electric field is primarily associated with the plasmoid motion and reconnection outflow. The non-ideal electric field is typically $\sim 0.1B_0$ (Guo et al. 2015; Liu et al. 2015, 2017) and the motional electric field is typically 5–10 times stronger compared to the non-ideal electric field. The non-ideal electric field is also present in the island region because of the non-zero

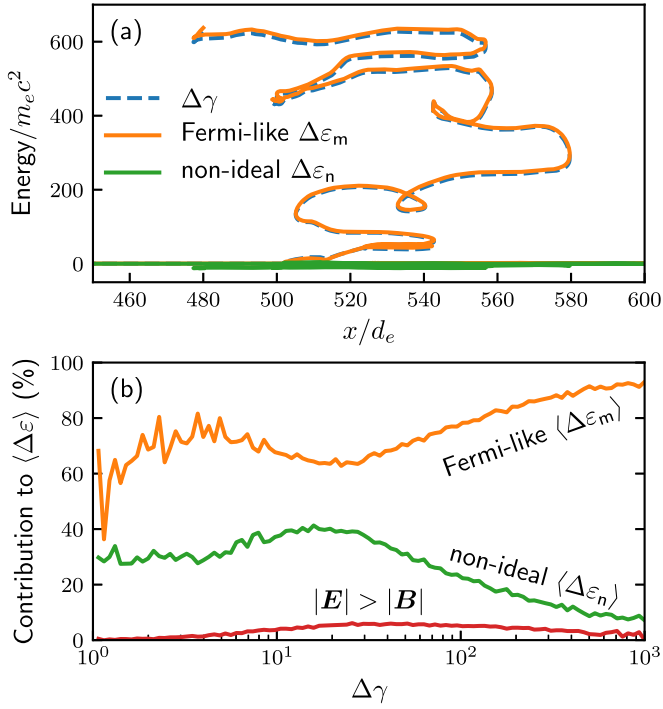


Figure 2. Panel (a) shows a sample particle accelerated with Fermi acceleration dominating over non-ideal electric field acceleration. The Fermi acceleration does not rely on initial direct acceleration. Panel (b) shows statistics of energy gain for ~ 1 million particles traced over the history of the simulation. The orange line shows the fraction of averaged energy gain from motional electric field as a function of energy gain until the end of simulation. The green line shows the contribution of the non-ideal electric field, and the red line shows the contribution of electric field in regions with $|E| > |B|$. The acceleration to high energy is dominated by the Fermi-type acceleration process.

divergence of pressure tensors in Equation (1). In the rest of this Letter we discuss the relative roles of motional electric field and non-ideal electric field in accelerating particles.

If the non-ideal electric field is essential for nonthermal acceleration in the reconnection layer, particles without significant direct acceleration would not be accelerated to high energy. We find that, however, while some high-energy particles experience an initial acceleration in the diffusion region with $|E| > |B|$, this process is not necessary because a significant number of high-energy particles did not pass through such regions (see below for more detailed discussions). Figure 2(a) shows the trajectory of a particle presented as energy gain versus x . The blue line represents the energy gain, the orange line shows the contribution from the motional electric field $\Delta\varepsilon_m$, and the green line indicates the contribution from the non-ideal electric field $\Delta\varepsilon_n$. This particle does not experience any significant non-ideal electric field acceleration and $\Delta\varepsilon_m$ dominates the energy increase (actually $\Delta\varepsilon_n < 0$ most of the time). However, the particle still gains a dramatic amount of energy and eventually reaches $\gamma \sim 600$. Meanwhile, we use ~ 1 million tracer particles and track their energy evolution. We calculate the contributions from the motional electric field $\Delta\varepsilon_m$ and non-ideal electric field $\Delta\varepsilon_n$ for each particle during the acceleration process. Figure 2(b) shows the averaged fractions of the energy gains from $\langle\Delta\varepsilon_m\rangle$ (orange), $\langle\Delta\varepsilon_n\rangle$ (green), and the region with $|E| > |B|$ (red) as a function of energy gain until the end of simulation. The contributions from motional and non-ideal electric fields are comparable at low energies, but Fermi-type acceleration becomes dominant

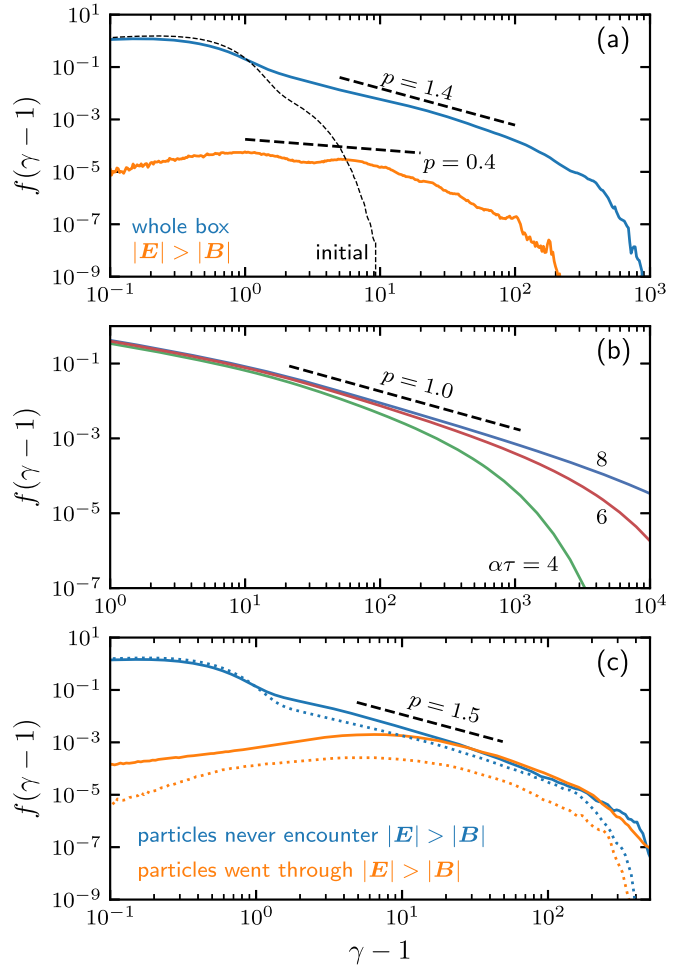


Figure 3. (a) Energy spectra for particles over the whole domain (blue) and only the regions with $|E| > |B|$ (orange). The spectral indices for the two regions are significantly different from each other. (b) Illustration showing Equation (3) for $\alpha\tau = 4, 6$, and 8 with $\delta = 0.4$, $\varepsilon_c = 10m_e c^2$ and $\tau_{esc} \rightarrow \infty$. A flat injected energy spectrum is steepened to $1 < p < 2$ by Fermi acceleration. (c) Energy spectra for particles that never experienced the region (blue) with $|E| > |B|$ and particles that encountered at least one such region (orange) before $\omega_{pet} = 400$ (dashed lines) and 640 (solid lines). The two energy spectra give similar indices at high energy.

when it accelerates particles to high energy, whereas the role of the non-ideal electric field is negligible. The effect of regions with $|E| > |B|$ is even smaller. This clearly demonstrates that the Fermi acceleration is the dominant mechanism for particle acceleration to high energy.

In Figure 3, we further examine the roles of the non-ideal electric field and motional electric field in forming the power-law distribution. Figure 3(a) shows the energy spectrum for particles in all of the diffusion regions with a strong non-ideal electric field and weak magnetic field $|E| > |B|$ and the energy spectrum integrated over the whole domain at $\omega_{pet} = 800$, respectively. Although quite variable, the representative energy spectrum in the diffusion region is nonthermal with a small spectral index $p \sim 0.4-0.5$ and an exponential cutoff around $\gamma \sim 10-20$. Meanwhile, the spectral index for the energy spectrum over the whole domain is approximately $p = 1.4$, which is consistent with previous works (Guo et al. 2014, 2015; Sironi & Spitkovsky 2014; Werner et al. 2016). While previous study has claimed that the energy spectra in the diffusion region and the whole reconnection domain are the

same (Sironi & Spitkovsky 2014), the analysis here shows a clear difference. To understand this difference, we examine the energy continuity equation with injection and escape of particles (Zenitani & Hoshino 2001; Drury 2012; Guo et al. 2014, 2015):

$$\frac{\partial f}{\partial t} + \frac{\partial}{\partial \varepsilon} \left(\frac{\partial \varepsilon}{\partial t} f \right) = \frac{f_{\text{inj}}}{\tau_{\text{inj}}} - \frac{f}{\tau_{\text{esc}}}, \quad (2)$$

where τ_{inj} and τ_{esc} are the injection and escape timescales for particles. We assume that some particles are pre-accelerated at X-points to a hard power-law with an exponential cutoff $f_{\text{inj}} = f_0 (\varepsilon/\varepsilon_0)^{-\delta} \exp(-\varepsilon/\varepsilon_c)$, where $\delta = 0.4$ is the spectral index, $\varepsilon_0 = m_e c^2$ and the cutoff energy is $\varepsilon_c = 10 m_e c^2$ based on Figure 3(a). Those particles are injected into island regions where particles are further accelerated by a Fermi-type process with acceleration rate $\alpha = \dot{\varepsilon}/\varepsilon$. The solution to (2) can be found by integrating Equation (2) along the characteristics from $t = 0$ to $t = \tau$ (Drury et al. 1999; Guo et al. 2014):

$$f(\tau) = \frac{f_0 \varepsilon_c^\theta}{\alpha \tau_{\text{inj}}} [\Gamma_\theta(b) - \Gamma_\theta(b e^{\alpha \tau})] \varepsilon^{-(1+\beta)}, \quad (3)$$

where $\beta = 1/(\alpha \tau_{\text{esc}})$, $\theta = 1 + \delta - \beta$, $b = \varepsilon_0/\varepsilon_c$, and $\Gamma_s(x)$ is the upper incomplete Gamma function. In the limit of large $\alpha \tau$ (strong acceleration), the resulting energy spectrum is a power law $f \propto \varepsilon^{-p}$ with $p = 1 + \beta$ in energy larger than the injected energy ε_c . We emphasize here that for generating a power-law distribution, the injected distribution does not have to be nonthermal (Guo et al. 2014) and the actual value of δ does not alter the resulting spectral index. The value of $\alpha \tau$ can be estimated in particle-in-cell (PIC) simulations (e.g., as described in Guo et al. 2014) and for our simulations we obtained that $\alpha \tau = \int_0^{\tau_{\text{inj}}} \alpha dt \sim 4$, where we have assumed that the injection time τ_{inj} lasts until the saturation of reconnection. In Figure 3(b) we plot Equation (3) for $\alpha \tau = 4, 6$, and 8 and $\tau_{\text{esc}} \rightarrow \infty$, as our simulations do not include particle escape from the domain. This model predicts that the spectrum is steepened by the Fermi acceleration with $1 < p < 2$, consistent with PIC simulation results. For the strong acceleration case ($\alpha \tau = 8$), the spectral index approaches $p = 1$, which is consistent with simulations for $\sigma \gg 1$ (Guo et al. 2014, 2015; Sironi & Spitkovsky 2014; Werner et al. 2016). These results suggest that Fermi acceleration does not require additional acceleration at X-points and the flat energy spectrum generated in X-lines is modified by Fermi acceleration within the outflow. We verify this by examining energy spectra for particles that never experience a diffusion region with $|E| > |B|$ and particles that did encounter at least one such region before $\omega_{pe} t = 400$ (dashed lines) and 640 (solid lines) in Figure 3(c). At $\omega_{pe} t = 400$, among the particles accelerated to $\gamma > 10$, only 25% of particles have encountered the regions with $|E| > |B|$. Particles that never encounter such a diffusion region still develop a clear power-law distribution. Later on, more particles went through the diffusion region but the spectral indices for these two classes of particles are still quite similar, confirming the basic conclusions from the analytical model. For sufficiently high energy ($\gamma \gtrsim 10$), the spectral indices for these two

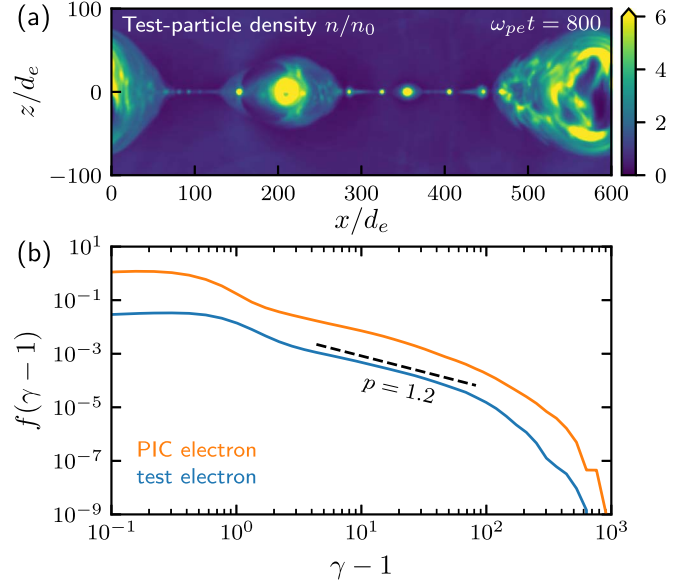


Figure 4. Evolution of a test-particle population that does not experience non-ideal electric field in the PIC simulation at $\omega_{pe} t = 800$. Panel (a) shows the test-particle density in a snapshot. Panel (b) shows the energy spectrum for the test-particle population. A power-law distribution with a spectral index that is similar to that of self-consistent electrons is developed, even excluding the non-ideal electric field.

classes of particles are quite similar, confirming the basic conclusions from the analytic model.

This analysis demonstrates that efficient Fermi acceleration does not require direct acceleration at X-lines. Furthermore, the energetic particles generated within the diffusion region are modified by the same Fermi-like process in the outflows. Ultimately, at high energy, the spectral indices are nearly the same, regardless of whether the particles ever encounter a diffusion region. This indicates that the nonthermal spectra resulting from relativistic magnetic reconnection can be computed by ignoring the influence of the non-ideal electric field. To directly demonstrate this, we performed an additional simulation with a test-particle electron component that does not feedback to the system. The test-particle electrons have the same initial distribution and one-tenth the number of particles of electrons that is self-consistently evolved in the simulation, but only experience the motional electric field \mathbf{E}_m during the simulation. While these test particles are not self-consistently evolved in the simulation, they do retain guiding-center drift motions such as electric field drift, grad-B drift, and curvature magnetic drift, and therefore can experience Fermi and betatron acceleration processes. This approach completely removes the acceleration associated with non-ideal electric field, but keeps Fermi-type acceleration in the reconnection layer. Figure 4(a) shows the density of test-particle population, and they are mainly concentrated in magnetic islands as expected. Figure 4(b) shows the energy spectrum for the test-particle component. Test-particle electrons develop a power-law-like energy spectrum similar to the self-consistent electrons in Figure 3(a). The main extent of the power-law distribution is still preserved with a cutoff energy $\gamma \sim 100$, indicating that it includes the main physics necessary for developing power-law distributions.




5. Discussion and Conclusion

The dominant acceleration mechanism in relativistic reconnection has been a controversial issue (Guo et al. 2014, 2015; Sironi & Spitkovsky 2014). Recently, Petropoulou & Sironi (2018) studied the long-term evolution of energy spectrum in large two-dimensional kinetic simulations of relativistic reconnection and found that the break energy sustainably increases and spectrum continuously softens. The determining acceleration process that they found is consistent with the current study and Guo et al. (2014, 2015). In general, the evolution of spectral index can be studied using the analysis that we proposed as well. However, we remark that effects like particle loss from more realistic boundary conditions as well as three-dimensional physics would be important to consider.

A major challenge for describing particle acceleration during magnetic reconnection in large-scale astrophysical system is the enormous scale separation between the system scales and plasma kinetic scales. The results of this Letter clearly demonstrate that the formation of power-law distributions does not rely on the non-ideal electric field. While the non-ideal electric field at X-points does accelerate a small population of particles, Fermi-type acceleration dominates over the direct acceleration and determines the spectral index. Therefore, the X-line acceleration may be parameterized as an additional injection process for further Fermi-type acceleration. For large-scale applications of reconnection, the non-ideal electric field is concentrated at boundary layers, and it may not be a significant source of energetic particles in a macroscopic reconnection event. This conclusion has profound implications for modeling particle acceleration in large-scale astrophysical systems, as it opens up the possibility of modeling the energetic particle spectra without resolving microscopic diffusion regions.

We gratefully acknowledge discussions with Joel Dahlin, Jim Drake, Sasha Philippov, Lorenzo Sironi, Anatoly Spitkovsky, and Marc Swisdak, and technical support in particle tracer analysis by Bin Dong and Suren Byna from Lawrence Berkeley National Lab (LBNL). We are grateful for support from DOE through the LDRD program at LANL and DoE/OFES support to LANL, and NASA ATP program through grant NNH17AE68I. X.L.'s contribution is in part supported by NASA under grant NNH16AC60I. The research by P.K. was also supported by the LANL through its Center for Space and Earth Science (CSES). CSES is funded by LANL's Laboratory Directed Research and Development (LDRD) program under project number 20180475DR. Simulations were performed at National Energy Research Scientific Computing Center (NERSC) and with LANL institutional computing.

ORCID iDs

Fan Guo  <https://orcid.org/0000-0003-4315-3755>
 William Daughton  <https://orcid.org/0000-0003-1051-7559>
 Patrick Kilian  <https://orcid.org/0000-0002-8906-7783>

Hui Li  <https://orcid.org/0000-0003-3556-6568>

References

- Abdo, A. A., Ackermann, M., Ajello, M., et al. 2011, *Sci*, **331**, 739
 Arons, J. 2012, *SSRv*, **173**, 341
 Beresnyak, A., & Li, H. 2016, *ApJ*, **819**, 90
 Bessho, N., & Bhattacharjee, A. 2005, *PhRvL*, **95**, 245001
 Bessho, N., & Bhattacharjee, A. 2012, *ApJ*, **750**, 129
 Birn, J., Artemyev, A. V., Baker, D. N., et al. 2012, *SSRv*, **173**, 49
 Bowers, K. J., Albright, B. J., Yin, L., Bergen, B., & Kwan, T. J. T. 2008, *PhPl*, **15**, 055703
 Cerutti, B., Werner, G. R., Uzdensky, D. A., & Begelman, M. C. 2013, *ApJ*, **770**, 147
 Dahlin, J. T., Drake, J. F., & Swisdak, M. 2014, *PhPl*, **21**, 092304
 Daughton, W., & Karimabadi, H. 2007, *PhPl*, **14**, 072303
 Daughton, W., Scudder, J., & Karimabadi, H. 2006, *PhPl*, **13**, 072101
 de Gouveia dal Pino, E. M., & Lazarian, A. 2005, *A&A*, **441**, 845
 Drake, J. F., Arnold, H., Swisdak, M., & Dahlin, J. T. 2019, *PhPl*, **26**, 012901
 Drake, J. F., Swisdak, M., Che, H., & Shay, M. A. 2006, *Natur*, **443**, 553
 Drury, L. O. 2012, *MNRAS*, **422**, 2474
 Drury, L. O., Duffy, P., Eichler, D., & Mastichiadis, A. 1999, *A&A*, **347**, 370
 Fu, X. R., Lu, Q. M., & Wang, S. 2006, *PhPl*, **13**, 012309
 Gary, D. E., Chen, B., Dennis, B. R., et al. 2018, *ApJ*, **863**, 83
 Giannios, D., Uzdensky, D. A., & Begelman, M. C. 2009, *MNRAS*, **395**, L29
 Guo, F., Li, H., Daughton, W., & Liu, Y.-H. 2014, *PhRvL*, **113**, 155005
 Guo, F., Li, X., Li, H., et al. 2016, *ApJ*, **818**, L9
 Guo, F., Liu, Y.-H., Daughton, W., & Li, H. 2015, *ApJ*, **806**, 167
 Hesse, M., & Zenitani, S. 2007, *PhPl*, **14**, 112102
 Hoshino, M., & Lyubarsky, Y. 2012, *SSRv*, **173**, 521
 Ji, H., & Daughton, W. 2011, *PhPl*, **18**, 111207
 Ji, H., Yamada, M., Hsu, S., & Kulsrud, R. 1998, *PhRvL*, **80**, 3256
 Kopp, R. A., & Pneuman, G. W. 1976, *SoPh*, **50**, 85
 Krucker, S., Hudson, H. S., Glesener, L., et al. 2010, *ApJ*, **714**, 1108
 le Roux, J. A., Zank, G. P., Webb, G. M., & Khabarova, O. 2015, *ApJ*, **801**, 112
 Li, X., Guo, F., & Li, H. 2019, *ApJ*, **879**, 5
 Li, X., Guo, F., Li, H., & Birn, J. 2018a, *ApJ*, **855**, 80
 Li, X., Guo, F., Li, H., & Li, G. 2017, *ApJ*, **843**, 21
 Li, X., Guo, F., Li, H., & Li, S. 2018b, *ApJ*, **866**, 4
 Liu, Y.-H., Guo, F., Daughton, W., Li, H., & Hesse, M. 2015, *PhRvL*, **114**, 095002
 Liu, Y.-H., Hesse, M., Guo, F., et al. 2017, *PhRvL*, **118**, 085101
 McKinney, J. C., & Uzdensky, D. A. 2012, *MNRAS*, **419**, 573
 Øieroset, M., Lin, R. P., Phan, T. D., Larson, D. E., & Bale, S. D. 2002, *PhRvL*, **89**, 195001
 Oka, M., Birn, J., Battaglia, M., et al. 2018, *SSRv*, **214**, 82
 Oka, M., Phan, T.-D., Krucker, S., Fujimoto, M., & Shinohara, I. 2010, *ApJ*, **714**, 915
 Petropoulou, M., & Sironi, L. 2018, *MNRAS*, **481**, 5687
 Phan, T. D., Kistler, L. M., Klecker, B., et al. 2000, *Natur*, **404**, 848
 Pritchett, P. L. 2006, *JGRA*, **111**, 10212
 Sironi, L., & Spitkovsky, A. 2014, *ApJ*, **783**, L21
 Swisdak, M., Liu, Y.-H., & Drake, J. F. 2008, *ApJ*, **680**, 999
 Tavani, M., Bulgarelli, A., Vittorini, V., et al. 2011, *Sci*, **331**, 736
 Uzdensky, D. A., Cerutti, B., & Begelman, M. C. 2011, *ApJ*, **737**, L40
 Wang, H., Lu, Q., Huang, C., & Wang, S. 2016, *ApJ*, **821**, 84
 Werner, G. R., Uzdensky, D. A., Cerutti, B., Nalewajko, K., & Begelman, M. C. 2016, *ApJ*, **816**, L8
 Zenitani, S., & Hoshino, M. 2001, *ApJ*, **562**, L63
 Zhang, B., & Yan, H. 2011, *ApJ*, **726**, 90
 Zhang, H., Chen, X., Böttcher, M., Guo, F., & Li, H. 2015, *ApJ*, **804**, 58
 Zhang, H., Li, X., Guo, F., & Giannios, D. 2018, *ApJ*, **862**, L25